

# Self-driving laboratory for accelerated discovery of thin-film materials

B. P. MacLeod<sup>1,3†</sup>, F. G. L. Parlane<sup>1,3†</sup>, T. D. Morrissey<sup>1,3</sup>, F. Häse<sup>4-7</sup>, L. M. Roch<sup>4-7</sup>, K. E. Dettelbach<sup>1</sup>, R. Moreira<sup>1</sup>, L. P. E. Yunker<sup>1</sup>, M. B. Rooney<sup>1</sup>, J. R. Deeth<sup>1</sup>, V. Lai<sup>1</sup>, G. J. Ng<sup>1</sup>, H. Situ<sup>1</sup>, R. H. Zhang<sup>1</sup>, A. Aspuru-Guzik<sup>4-8\*</sup>, J. E. Hein<sup>1\*</sup>, C. P. Berlinguette<sup>1-3,8\*</sup>

<sup>1</sup>*Department of Chemistry, The University of British Columbia, Vancouver, British Columbia, Canada*

<sup>2</sup>*Department of Chemical & Biological Engineering, The University of British Columbia, Vancouver, British Columbia, Canada*

<sup>3</sup>*Stewart Blusson Quantum Matter Institute, The University of British Columbia, Vancouver, British Columbia, Canada*

<sup>4</sup>*Department of Chemistry and Chemical Biology, Harvard University, Cambridge, Massachusetts, USA*

<sup>5</sup>*Department of Chemistry, University of Toronto, Toronto, Ontario, Canada*

<sup>6</sup>*Department of Computer Science, University of Toronto, Toronto, Ontario, Canada*

<sup>7</sup>*Vector Institute for Artificial Intelligence, MaRS Centre, Toronto, Ontario, Canada*

<sup>8</sup>*Canadian Institute for Advanced Research (CIFAR), MaRS Centre, Toronto, Ontario, Canada*

†These authors contributed equally to this work

Email: cberling@chem.ubc.ca, alan@aspuru.com, jhein@chem.ubc.ca

Clean energy technologies are notoriously slow to commercialize because discovering and optimizing new materials for applications typically takes over a decade<sup>1</sup>. Self-driving laboratories that iteratively design, execute, and learn from experiments in a fully autonomous loop present an opportunity to accelerate the materials discovery and optimization process<sup>2,3</sup>. We report here a self-driving modular robotic platform capable of optimizing thin films common to energy conversion, storage, and conservation technologies. This materials acceleration platform (MAP<sup>4</sup>) is capable of autonomously modulating the optical and electronic properties of thin films by modifying the film composition, deposition parameters, and annealing conditions. The platform is driven by a machine learning (ML) algorithm suitable for high-dimensional optimization<sup>5,6</sup>. We demonstrate this MAP by using it to maximize the hole mobility of organic hole transport materials (HTMs) for use in perovskite solar cells (PSCs)<sup>7</sup>. An unexpected outcome of this optimization process was the finding that highly-doped HTM compositions can enhance the thermal stability of HTM films. These results demonstrate the possibilities of using autonomous laboratories to discover organic and inorganic materials relevant to clean energy technologies.

Optimizing the properties of thin films is time intensive because of the infinite number of compositional, deposition, and processing parameters available<sup>1,4</sup>. These parameters are often correlated and can have a profound effect on the structure and physical properties of the film and any adjacent layers present in a device<sup>8</sup>. There exist few computational tools available for predicting the properties of materials with compositional and structural disorder, and thus the materials discovery process still relies heavily on empirical data. High-throughput experimentation (HTE) is an established method for sampling a large parameter space<sup>9,10</sup>, but it is nearly impossible to sample the full set of combinatorial parameters available for thin films. Parallelized methodologies are also constrained by the experimental techniques that can be used effectively in practice. The overwhelming size of the thin film materials parameter space motivates the need for both data- and theory-guided algorithms for executing experiments beyond what can be achieved with HTE alone<sup>3,11,12</sup>.

The experimental approach of iterating between automated experimentation and machine-learning-based experiment planning has resulted in early successes in addressing high-dimensional problems in experimental physics<sup>13</sup>, chemistry<sup>14</sup>, and life-sciences<sup>15</sup>. This approach is only starting to be implemented in the materials sciences<sup>4</sup>, as demonstrated by the optimization of carbon nanotube growth<sup>2</sup>, amorphous alloy compositions<sup>16</sup>, and inorganic perovskite quantum dot nucleation<sup>11</sup>. We demonstrate here the optimization of thin films using our platform named “*Ada*”, a flexible and modular self-driving laboratory capable of autonomously synthesizing, processing, and characterizing organic thin films. *Ada* trains itself how to find target parameters without any prior knowledge enabling iterative experimental designs that maximize the information gain per sample (Fig. 1).

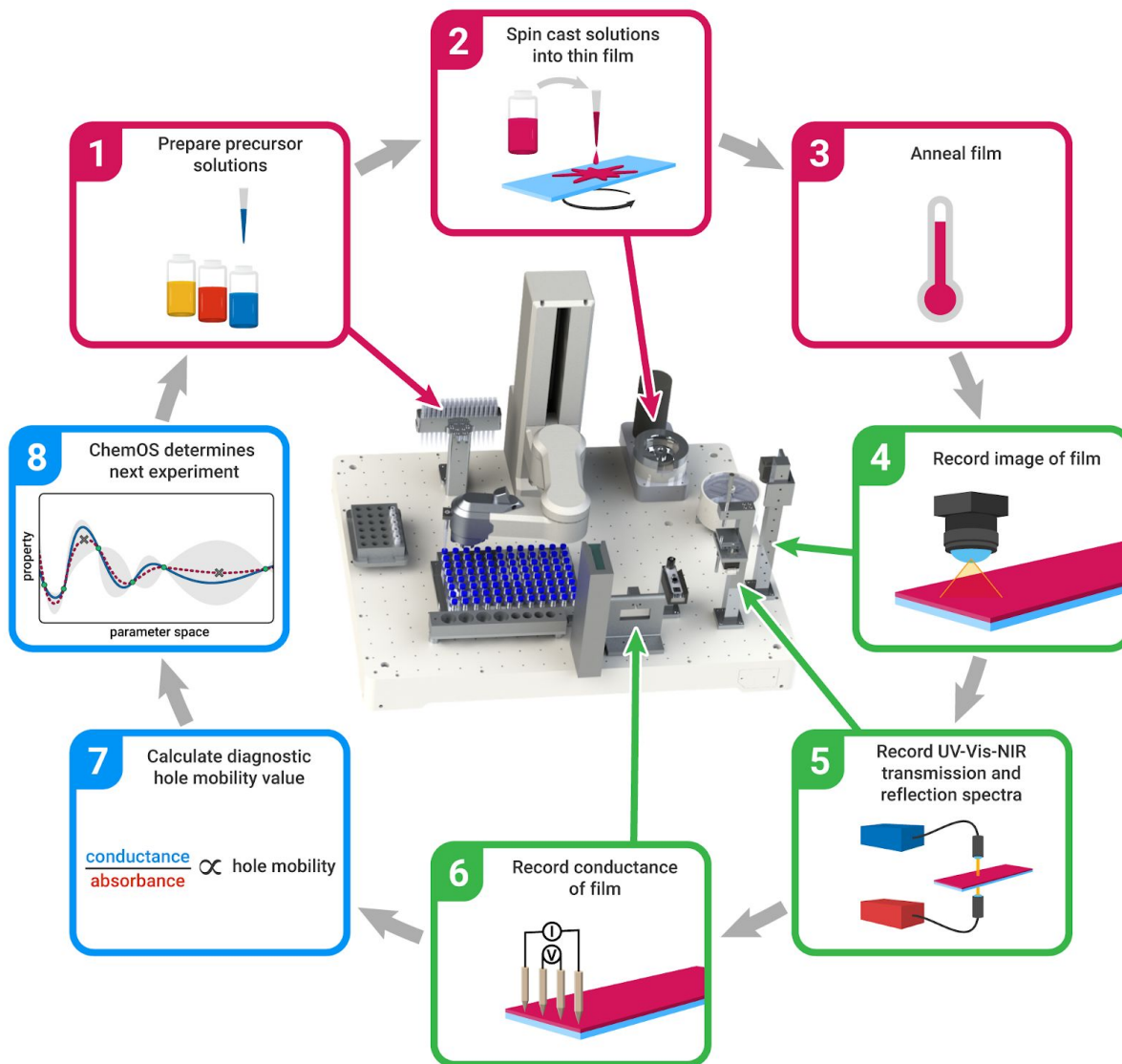


**Fig 1 | *Ada* employs an autonomous optimization workflow.** The self-driving laboratory is based on a modular North Robotics N9 robot (centre) and the *Phoenix*<sup>5</sup> Bayesian optimization algorithm. The robotic arm is equipped with a multi-purpose gripper and a fluid probe connected to a syringe pump (not shown) for performing precision pipetting of solutions. The gripper enables interaction with a variety of objects such as vials, a spin coater, and a vacuum-based substrate handler. The autonomous workflow involves iterative experimentation with the goal of discovering a thin film composition with the highest possible “pseudomobility”. Each iteration of the workflow involves (1) mixing an HTM-dopant-additive solution, (2) spin coating the solution onto a substrate, (3) thermally annealing for a variable amount of time, (4) imaging with a visible-light camera, (5) acquiring UV-Vis-NIR spectra in reflection and transmission modes, (6) measuring the I-V curve of the film with a 4-point probe, (7) computing a pseudomobility based on the IV and spectroscopic data, and (8) feeding this pseudomobility into the *ChemOS*<sup>6</sup> orchestration software and the *Phoenix* optimization algorithm which then designs the next experiment.

As a first step in proving out the methodology, we designed *Ada* to target organic hole and electron transport layers that are ubiquitous in advanced solar cells<sup>17</sup>, as well as optoelectronics applications such as organic lasers<sup>18</sup> and light emitting diodes<sup>19</sup>. We built *Ada* specifically to optimize the hole mobility of spiro-OMeTAD, an organic HTM common to perovskite solar cells (PSCs)<sup>20</sup>. The hole mobility of spiro-OMeTAD is critical to PSC performance, but it is highly sensitive to dopants, additives, spin-coating solvents, and post-deposition processing<sup>20–24</sup>. How each of these factors affect the hole mobility of

amorphous spiro-OMeTAD remains difficult to model<sup>8,25</sup>, and thus optimizing the relevant properties of spiro-OMeTAD is still done empirically. This optimization process often takes months to complete and slows the translation of new organic hole and electron transport layers for solar cells and related devices.

*Ada* autonomously optimizes the hole mobility of spiro-OMeTAD by: (i) measuring and mixing solutions of HTMs, dopants, and plasticizers; (ii) depositing solutions as thin films on rigid substrates; (iii) imaging each film to detect morphologies, defects, and impurities; and (iv) characterizing the optical and conductivity properties to produce surrogate hole mobility data. This data is received by *ChemOS*<sup>6</sup>, which uses the *Phoenix*<sup>5</sup> global Bayesian optimization algorithm to design new experiments by actively learning from previously acquired data. *Phoenix* uses a sampling parameter to explicitly bias experimental design towards exploration or exploitation in an alternating fashion, and has been shown to outperform random and systematic searches<sup>5,6,26</sup>. The platform aspirates, dispenses, and mixes liquid precursors with the assistance of syringe pump and a weigh scale. Precursor solutions are spin-cast as thin films on glass substrates, which can then be annealed up to 165 °C using a forced convection annealing system. *Ada* then characterizes the films using purpose-built systems for dark field photography, UV-Vis-NIR reflection and transmission spectroscopy, and 4-point probe conductance. The robot also serves as a XYZ sample-positioning stage enabling all characterizations to be performed at multiple positions on the sample, which we leverage to collect spectroscopy and conductance data at 7 spatial positions on each sample. The ability to produce high quality, well-organized datasets while also enabling typically uncontrolled variables (e.g., time between process steps, height of spin coating dispense nozzle) to become controlled or optimization parameters are very powerful features of *Ada*. Moreover, *Ada* is controlled using flexible, open-source Python software (see Supplementary Information), which facilitates the rapid implementation of new experiments.

We selected HTM hole mobility as our target parameter for optimization, but this parameter typically requires assembly of multilayer devices in order to get a valid measurement<sup>25</sup>. Conventional methods are simply not compatible with the time scale needed for efficient autonomous optimization<sup>27</sup>. We therefore developed a scheme where we could use 4-point-probe conductivity and UV-Vis-NIR spectroscopy measurements to produce a diagnostic quantity, “pseudomobility”, that is proportional to hole mobility (see Supplementary Information). Pseudomobility is the quotient of the sheet conductance of a thin film and the absorbance of oxidized spiro-OMeTAD in the film. This ratio, which provides a thickness-independent low latency analytical surrogate for hole mobility, became our target optimization objective.

The pseudomobilities of spiro-OMeTAD thin films were optimized by iteratively designing film compositions with variable annealing times and concentrations of dopant. Solutions prepared from stock solutions of spiro-OMeTAD and a cobalt(III) dopant (along with a fixed amount of the plasticizer, 4-*tert*-butylpyridine) were spin-coated onto substrates to yield thin films. Each film was annealed, imaged, and analyzed to determine a pseudomobility value that was relayed to *ChemOS*. Fig. 2a chronicles how the doping ratios and annealing times were varied during optimization for two independent experimental campaigns. An important outcome is that both campaigns converged on the same global maximum for both doping ratio (~0.4 eq.) and annealing time (~75 s) to deliver films with the same maximum pseudomobilities. This reproducible endpoint is significant and demonstrates that *Ada* can successfully navigate a broad experimental space.

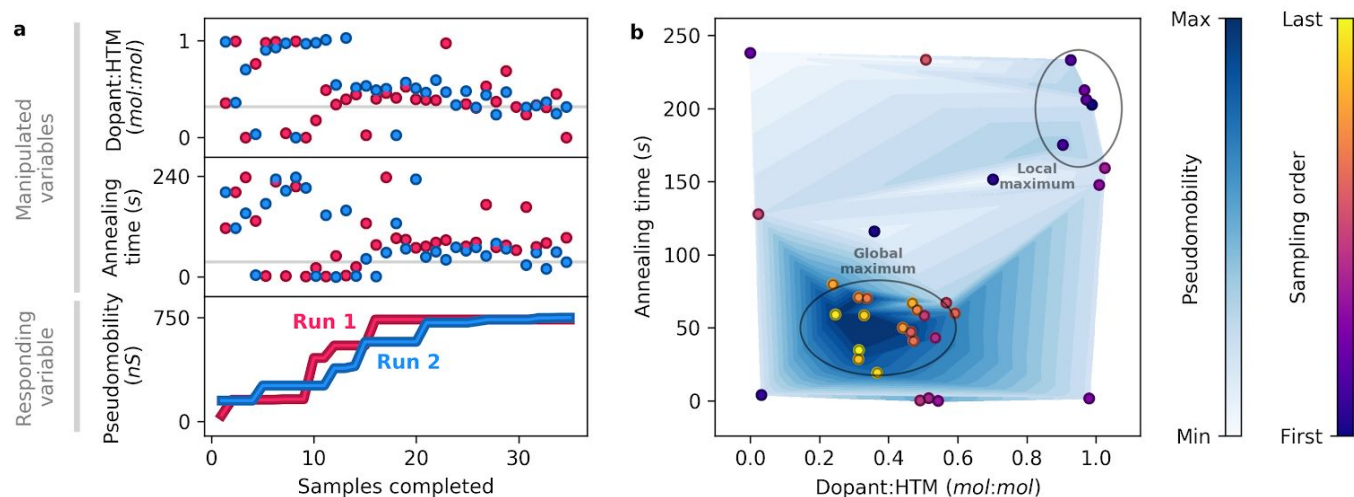


**Fig. 2 | Results of thin film pseudomobility optimization carried out by the self-driving lab.** **a**, Experimental values for cobalt doping ratio, annealing time, and maximum measured pseudomobility as a function of the number of experiments performed for two independent optimization runs. **b**, The pseudomobility response surface and sampled points for the second (blue, left) optimization run. The algorithm initially discovered a local maximum, and then discovered the global maximum of the sampled parameter space.

Fig. 2b shows the locations and sequence of the experimentally sampled points in the parameter space. The sampled points can be seen to initially cluster at a local maximum ( $\sim 100\%$  doping and annealing time  $> 200$  s) prior to finding a higher performance region elsewhere in the parameter space. While the eventual rejection of the local maximum confirms that the *explore-exploit* functionality of *Phoenix* can prevent the search from becoming stuck near local optima, we were curious why *Ada* identified a local maximum at high doping levels. Subsequent investigations of the dark field images of these films revealed annealing-induced dewetting of the films containing intermediate amounts of dopant. At elevated doping levels, dewetting was suppressed, allowing a region of improved thermal stability to be identified (see Supplementary Information). The favourable performance of high dopant/high annealing time films was not intuitive<sup>28</sup>, and was only discovered because the autonomous platform facilitated a search within a larger range of doping and annealing conditions than is typically explored in studies of organic HTMs. This result represents a rational scientific finding from an artificially intelligent experimental design.

We report here the first use of a self-driving laboratory to optimize composition and processing parameters for thin film materials. This proof-of-principle study targeted the optimization of a type of thin organic semiconducting film common to advanced solar cells, but the modularity of our robotic platform and control software enables the rapid incorporation of new experiments, techniques, analytical hardware, and algorithms. The *Ada* platform can therefore be easily tailored for a range of inorganic and organic materials and applications, and even be coupled to automated organic synthesis methodologies developed for the pharmaceutical industry<sup>29,30</sup>. We contend that expanding the capabilities of autonomous experimental platforms like *Ada* will accelerate the optimization of multi-layered materials and devices common to clean energy technologies.

## References

1. Correa-Baena, J.-P. *et al.* Accelerating materials development via automation, machine learning, and high-performance computing. *Joule* **2**, 1410–1420 (2018).
2. Nikolaev, P., Hooper, D., Perea-López, N., Terrones, M. & Maruyama, B. Discovery of wall-selective carbon nanotube growth conditions via automated experimentation. *ACS Nano* **8**, 10214–10222 (2014).
3. Häse, F., Roch, L. M. & Aspuru-Guzik, A. Next-generation experimentation with self-driving laboratories. *Trends in Chemistry* **1**, 282–291 (2019).
4. Aspuru-Guzik, A. *et al.* *Materials Acceleration Platform: Accelerating Advanced Energy Materials Discovery by Integrating High-Throughput Methods and Artificial Intelligence*. (Mission Innovation Clean Energy Materials Innovation Challenge, 2018).
5. Häse, F., Roch, L. M., Kreisbeck, C. & Aspuru-Guzik, A. Phoenix: a bayesian optimizer for chemistry. *ACS Cent Sci* **4**, 1134–1145 (2018).
6. Roch, L. M. *et al.* ChemOS: Orchestrating autonomous experimentation. *Science Robotics* **3**, eaat5559 (2018).
7. Bakr, Z. H. *et al.* Advances in hole transport materials engineering for stable and efficient perovskite solar cells. *Nano Energy* **34**, 271–305 (2017).
8. Cao, B. *et al.* How to optimize materials and devices via design of experiments and machine learning: demonstration using organic photovoltaics. *ACS Nano* **12**, 7434–7444 (2018).
9. Xiang, X. D. *et al.* A combinatorial approach to materials discovery. *Science* **268**, 1738–1740 (1995).
10. Stein, H. S., Guevarra, D., Newhouse, P. F., Soedarmadji, E. & Gregoire, J. M. Machine learning of optical properties of materials - predicting spectra from images and images from spectra. *Chem. Sci.* **10**, 47–55 (2019).
11. Li, J. *et al.* AIR-Chem: authentic intelligent robotics for chemistry. *J. Phys. Chem. A* **122**, 9142–9148

- (2018).
12. Bai, Y. *et al.* Accelerated discovery of organic polymer photocatalysts for hydrogen evolution from water through the integration of experiment and theory. *J. Am. Chem. Soc.* **141**, 9063–9071 (2019).
  13. Gopalswamy, V. *et al.* Tripled yield in direct-drive laser fusion through statistical modelling. *Nature* **565**, 581–586 (2019).
  14. Milo, A., Bess, E. N. & Sigman, M. S. Interrogating selectivity in catalysis using molecular vibrations. *Nature* **507**, 210–214 (2014).
  15. King, R. D. *et al.* Functional genomic hypothesis generation and experimentation by a robot scientist. *Nature* **427**, 247–252 (2004).
  16. Ren, F. *et al.* Accelerated discovery of metallic glasses through iteration of machine learning and high-throughput experiments. *Sci Adv* **4**, 1566 (2018).
  17. Meng, L. *et al.* Organic and solution-processed tandem solar cells with 17.3% efficiency. *Science* **361**, 1094–1098 (2018).
  18. Sandanayaka, A. S. D. *et al.* Indication of current-injection lasing from an organic semiconductor. *Appl. Phys. Express* **12**, 061010 (2019).
  19. Jhulki, S. & Moorthy, J. N. Small molecular hole-transporting materials (HTMs) in organic light-emitting diodes (OLEDs): structural diversity and classification. *J. Mater. Chem.* **6**, 8280–8325 (2018).
  20. Yang, X., Wang, H., Cai, B., Yu, Z. & Sun, L. Progress in hole-transporting materials for perovskite solar cells. *J. Mater. Chem. A Mater. Energy Sustain.* **27**, 650–672 (2018).
  21. Burschka, J., Kessler, F., Nazeeruddin, M. K. & Grätzel, M. Co(III) complexes as p-dopants in solid-state dye-sensitized solar cells. *Chemistry of Materials* **25**, 2986–2990 (2013).
  22. Wang, S. *et al.* Role of 4-tert-butylpyridine as a hole transport layer morphological controller in perovskite solar cells. *Nano Lett.* **16**, 5594–5600 (2016).

23. Bu, T. *et al.* Synergic interface optimization with green solvent engineering in mixed perovskite solar cells. *Adv. Energy Mater.* **7**, 1700576 (2017).
24. Fang, Y., Wang, X., Wang, Q., Huang, J. & Wu, T. Impact of annealing on spiro-OMeTAD and corresponding solid-state dye sensitized solar cells. *Phys. Status Solidi* **211**, 2809–2816 (2014).
25. Friederich, P. *et al.* Molecular origin of the charge carrier mobility in small molecule organic semiconductors. *Adv. Funct. Mater.* **26**, 5757–5763 (2016).
26. Häse, F., Roch, L. M. & Aspuru-Guzik, A. Chimera: enabling hierarchy based multi-objective optimization for self-driving laboratories. *Chem. Sci.* **9**, 7642–7655 (2018).
27. Brandt, R. E. *et al.* Rapid photovoltaic device characterization through bayesian parameter estimation. *Joule* **1**, 843–856 (2017).
28. Schloemer, T. H., Christians, J. A., Luther, J. M. & Sellinger, A. Doping strategies for small molecule organic hole-transport materials: impacts on perovskite solar cell performance and stability. *Chem. Sci.* **10**, 1904–1935 (2019).
29. Bédard, A.-C. *et al.* Reconfigurable system for automated optimization of diverse chemical reactions. *Science* **361**, 1220–1225 (2018).
30. Kitson, P. J. *et al.* Digitization of multistep organic synthesis in reactionware for on-demand pharmaceuticals. *Science* **359**, 314–319 (2018).

## Acknowledgments

The authors thank Natural Resources Canada (EIP2-MAT-001) for their financial support. C. P. B. is grateful to the Canadian Natural Science and Engineering Research Council (RGPIN 337345-13), Canadian Foundation for Innovation (229288), Canadian Institute for Advanced Research (BSE-BERL-162173), and Canada Research Chairs for financial support. B. P. M., F. G. L. P., T. D. M., and C. P. B. acknowledge support from the SBQMI's Quantum Electronic Science and Technology Initiative, the Canada First Research Excellence Fund, and the Quantum Materials and Future Technologies Program. J. E. H. is supported by the Canadian Natural Science and Engineering Research Council (RGPIN 2016-04613) and Canada Foundation for Innovation (35833). V. L., and H. S. were supported by an NSERC Strategic Partnership Grant (STPGP 493833-16). F. H. acknowledges support from the Herchel Smith Graduate Fellowship and the Jaques-Emile Dubois Student Dissertation Fellowship. L. M. R., and A. A.-G. were supported by the Tata Sons Limited Alliance Agreement (A32391) and the Office of Naval Research (N00014-19-1-2134), and would also like to thank Dr. Anders Frøseth for generous support. The authors would like to acknowledge Maddie Eghtesad for her contributions to the project hardware and experimentation and to Tara Zepel for her contributions in literature research. We thank the UBC Chemistry machine shop for assistance with instrument fabrication. We would like to acknowledge CMC Microsystems for the provision of products and services that facilitated this research, including SolidWorks 2018 SP5.0. For robot control and data processing, we would like to acknowledge the contributors to the Python programming language (Python Software Foundation, <https://www.python.org>).

## Author contributions

A.A-G., J. E. H. and C. P. B. conceived of and supervised the project. B. P. M., M. R., H. S., G. J. N., R. H. Z., and F. G. L. P. developed the robotic hardware. F. G. L. P., T. D. M., J. R. D., and B. P. M. developed the data analysis software. L. P. E. Y., B. P. M., F. G. L. P., G. J. N., R. H. Z., V. L., and H. S. developed the robotic control software. F. H., L. M. R., and A. A.-G. developed the optimization algorithm and interfaced the algorithm with the robot. F. G. L. P., T. D. M., B. P. M., F. H., and L. M. R. designed and performed the experiments. All authors participated in the writing of the manuscript.

## Author Information

**Competing interests.** The authors declare no competing interests.

**Correspondence.** Correspondence and requests for materials should be addressed to [cberling@chem.ubc.ca](mailto:cberling@chem.ubc.ca).

# Self-driving laboratory for accelerated discovery of thin-film materials

## *Supplementary information*

B. P. MacLeod<sup>1,3†</sup>, F. G. L. Parlane<sup>1,3†</sup>, T. D. Morrissey<sup>1,3</sup>, F. Häse<sup>4-7</sup>, L. M. Roch<sup>4-7</sup>, K. E. Dettelbach<sup>1</sup>, R. Moreira<sup>1</sup>, L. P. E. Yunker<sup>1</sup>, M. B. Rooney<sup>1</sup>, J. R. Deeth<sup>1</sup>, V. Lai<sup>1</sup>, G. J. Ng<sup>1</sup>, H. Situ<sup>1</sup>, R. H. Zhang<sup>1</sup>, A. Aspuru-Guzik<sup>4-8\*</sup>, J. E. Hein<sup>1\*</sup>, C. P. Berlinguette<sup>1-3,8\*</sup>

<sup>1</sup>*Department of Chemistry, The University of British Columbia, Vancouver, British Columbia, Canada*

<sup>2</sup>*Department of Chemical & Biological Engineering, The University of British Columbia, Vancouver, British Columbia, Canada*

<sup>3</sup>*Stewart Blusson Quantum Matter Institute, The University of British Columbia, Vancouver, British Columbia, Canada*

<sup>4</sup>*Department of Chemistry and Chemical Biology, Harvard University, Cambridge, Massachusetts, USA*

<sup>5</sup>*Department of Chemistry, University of Toronto, Toronto, Ontario, Canada*

<sup>6</sup>*Department of Computer Science, University of Toronto, Toronto, Ontario, Canada*

<sup>7</sup>*Vector Institute for Artificial Intelligence, MaRS Centre, Toronto, Ontario, Canada*

<sup>8</sup>*Canadian Institute for Advanced Research (CIFAR), MaRS Centre, Toronto, Ontario, Canada*

†These authors contributed equally to this work

Email: cberling@chem.ubc.ca, alan@aspuru.com, jhein@chem.ubc.ca

<b>Supplementary Methods</b>	<b>3</b>
Materials	3
Preparation of reagent solutions	3
Preparation of substrates	3
Robotic methods	3
Robotic preparation of substrate precursor solutions	3
Robotic spin coating of thin film samples	4
Thermal processing of thin film samples	4
Dark field photography	4
UV-Vis-NIR instrumentation	4
UV-Vis-NIR characterization and processing	5
4-point probe conductance instrumentation and characterization	5
UV-Vis-NIR data processing	5
Pseudomobility	6
<b>Supplementary Tables</b>	<b>8</b>
Sample data table for each campaign	8
<b>Supplementary Data</b>	<b>11</b>
Supplemental figures	11
<b>References</b>	<b>16</b>

# Supplementary Methods

## Materials

Acetonitrile (CAS 75-05-8, HPLC grade,  $\geq 99.9\%$ ), toluene (CAS 108-88-3, ACS grade), acetone (CAS 67-64-1, ACS grade), spiro-OMeTAD (CAS 207739-72-8, HPLC grade, 99%), FK 102 Co(III) TFSI salt (Sigma Aldrich product number 805203, 98%), and 4-*tert*-butylpyridine (CAS 3978-81-2, 96%) were purchased from Sigma Aldrich and were used without further purification. Extran<sup>®</sup> 300 detergent (EX0996-1) and 2-propanol (ACS grade,  $\geq 99.5\%$ ) were purchased from EMD Millipore Corporation and were used without further purification. Microscope slide substrates ( $75 \times 25 \times 1$  mm, VWR Cat. No. 16004-430) were purchased from VWR International.

## Preparation of reagent solutions

All reagent solutions were prepared in an atmosphere dried over anhydrous calcium sulfate (DRIERITE<sup>®</sup>), resulting in  $\sim 0.005$  mg/L of water remaining in the atmosphere. Toluene and acetonitrile solvents were prepared by drying over anhydrous magnesium sulfate, filtering through a  $0.2 \mu\text{m}$  PTFE filter, and stored over  $3 \text{ \AA}$  molecular sieves. A solution of 1:1 v/v solution of acetonitrile/toluene (MeCN/MePh) was prepared by mixing equal volumes of dry acetonitrile and toluene. A stock solution of spiro-OMeTAD was prepared by briefly (1-5 min) sonicating a mixture of spiro-OMeTAD (off-white powder) with MeCN/MePh. The resulting solution had a transparent, pale yellow color. A stock solution of FK 102 Co(III) TFSI salt was prepared by dissolving FK102 Co(III) TFSI salt (bright orange crystalline powder) in MeCN/MePh and stored without exposure to UV-light. The resulting solution had a transparent bright orange color. A stock solution of 4-*tert*-butylpyridine was prepared by dissolving *tert*-butylpyridine (clear, colorless solution) in MeCN/MePh. All stock solutions were prepared at concentrations of 50 mg solute per 1 mL solvent.

## Preparation of substrates

$75 \times 25 \times 1$  mm microscope slide substrates were cleaned through multi-step sonication. First, the slides were sonicated for 10 min in a 5% v/v solution of Extran<sup>®</sup> in deionized water. The slides were then sonicated sequentially in deionized water, acetone, and 2-propanol for 10 minutes each step. The slides were stored in 2-propanol and dried with filtered air before use.

## Robotic methods

The robot used is a Selective Compliance Assembly Robot Arm (SCARA)-type robot (*N9*, North Robotics; [www.northrobotics.com](http://www.northrobotics.com)) which performs the robotic manipulations in our workflows. This robot is driven by a controller (*C9*, North Robotics), which also provides auxiliary controls for third-party instruments and components used by the robot. The controller and additional peripherals are controlled by a computer running a Python script.

## Robotic preparation of substrate precursor solutions

The precursor solution for each sample was prepared by mixing varying amounts of: spiro-OMeTAD stock solution; FK 102 Co(III) TFSI salt stock solution; and 4-*tert*-butylpyridine stock solution in ambient conditions. In each precursor solution the FK 102 Co(III) TFSI:spiro-OMeTAD ratio (*n/n*) was between 0 to 1, with the ratio determined by the ChemOS orchestration software. The ratio (*m/m*) of *tert*-butylpyridine to the total amount of spiro-OMeTAD and FK102 Co(III) TFSI was fixed at 0.2. The resulting precursor solutions became dark purple in appearance upon the combination

of the spiro-OMeTAD and FK 102 Co(III) TFSI solutions. The precursor solutions were mixed through aspiration and were used within a minute of preparation.

## Robotic spin coating of thin film samples

The thin film samples were prepared via spin-coating with a custom-built spin-coater provided by North Robotics. The microscope slides were spun at 1000 rpm and 0.100 mL of the precursor solution was dispensed at a normal incidence at the center of the slide. Rotation continued for 60 s.

## Thermal processing of thin film samples

The forced convection annealing furnace was constructed from a MHT Products Inc. model 750 heat gun facing upward into a vertically oriented  $75 \times 50$  mm rectangular aluminum tube kept under ambient conditions. A  $40 \times 5$  mm sample port was cut 40 mm from the heat gun. Freshly spin coated thin film samples were moved by the N9 slide gripper into the furnace via the sample port, after which the heat gun power was triggered for the amount of time requested by the orchestration software. The temperature profile of the annealing procedure is shown in Supplementary Fig 2. The temperature of the slide ramps from ambient temperature to  $165\text{ }^{\circ}\text{C}$  over the first 100 s and remains at that temperature for the rest of the annealing time. After the requested heating time has elapsed, the arm immediately removed the sample from the furnace and held 25 mm above a 4500 rpm cooling fan for 3 min. This cooling period allowed samples to return to ambient temperature, regardless of annealing time, before further characterization.

## Dark field photography

Thin film samples were imaged at a dark field photography station composed of a FLIR Blackfly S Mono 12 MP USB Vision (Sony IMX226) camera mounted above an AmScope MIC-209 3 W ring light. The sample was moved by the robotic arm to 90 mm below the camera and illuminated by the ring light to provide contrast between smooth and rough regions of the film. Images were captured at three different overlapping locations at a resolution of  $4000 \times 3000$  px. Manual post-experiment analysis of collected images was used to identify dust, defects, and dewetting in thin film samples.

## UV-Vis-NIR instrumentation

UV-Vis-NIR transmission and reflection spectra were collected with a custom-built, fiber-optic spectroscopy station. A BLACK-Comet UV-Vis Spectrometer (190 - 900 nm,  $< 1$  nm resolving resolution), a DWARF-Star Miniature NIR Spectrometer (900 - 1700 nm, 2.5 nm resolving resolution), and two SL4 High Power Tungsten Halogen and Deuterium Lamps (190 - 2500 nm spectral range, 3000 K) were purchased from StellarNet, Inc. The visible portion of the lamps were operated on the third color temperature setting. A 3-way split fiber-optic reflection probe was positioned above and normal to the surface of the sample, which was connected to the BLACK-Comet spectrometer, the DWARF-Star spectrometer, and an SL4 lamp (reflection lamp). A collimating lens was positioned below and normal to the surface of the sample, and was connected to the second SL4 lamp (transmission lamp) via a second fiber-optic cable. A mechanical shutter was placed between the collimating lens and the sample, which was darkened with black flocked paper (Thor Lab part number BFP1). The BLACK-Comet UV-Vis and DWARF-STAR Miniature NIR spectrometers were controlled by a Raspberry Pi 3 Model B+ (2017) running Raspbian Stretch (Kernel 4.14) and Python 2.7.0. The SL4 lamps were controlled by an Arduino Due (A000062), which was slaved to the Raspberry Pi.

To perform a transmission measurement the mechanical shutter was opened, the upper reflection lamp internal shutter was closed, and the lower transmission lamp internal shutter was opened. To perform a reflection measurement the mechanical

shutter was closed, the lower transmission lamp internal shutter was closed, and the upper reflection lamp internal shutter was opened.

## UV-Vis-NIR characterization and processing

A  $75 \times 25 \times 1$  mm glass slide coated with 50 nm aluminum was purchased from Deposition Research Lab Inc. for use as a reflectance baseline. The true specular reflectance of the prepared reference sample was measured with an Agilent Cary 7000 Universal Measurement Spectrometer (UMS) using the Cary Universal Measurement Accessory (UMA) to hold the sample at  $10^\circ$  from normal. The sensitivity of the BLACK-Comet and DWARF-Star spectrometers were set by increasing the integration time (in ms) of the detectors until the signal was between 80% and 95% of saturation, where saturation was  $2^{16}$  counts. For transmission measurements, the sensitivity was determined with no sample present, and for reflection measurements, the sensitivity was determined with the calibrated aluminum mirror. The bright and dark baselines for transmission were completed with no sample present and with the transmission lamp on and off, respectively. The bright and dark baselines for reflection were completed with the calibrated aluminum mirror present and with the reflection lamp on and off, respectively. The known true reflection of the aluminum mirror, obtained from the Cary 7000, was used to define the bright reflection baseline.

For each film fabricated, four UV-Vis-NIR spectra were collected. First the reflection and transmission spectra of a blank glass substrate were collected, followed by analogous reflection and transmission spectra of the annealed thin film on an identical substrate. The spectra of the uncoated and coated substrate were used to approximate the absorbance of the thin film, as described in the *UV-Vis-NIR data processing* section.

## 4-point probe conductance instrumentation and characterization

4-point probe conductivity measurements were performed with a Keithley Series K2636B System SourceMeter<sup>®</sup> Instrument with a Signatone Four Point Probe Head (part number SP4-40045TBN, 0.040" tip spacing, 45 gram pressure, tungsten carbide tips with 0.010" radii) connected through a Signatone Triax to BNC feedthrough panel (part number TXBA-M160-M).

The current on the outer probes was stepped from 0 to 4 nA in 0.8 nA steps. The system was stabilized at each step for 0.5 s, and the potential across the inner probes was integrated for 25 power line cycles (at 60 Hz). The slope of the potential as a function of the current sourced afforded the resistance. No correction factors were applied to the resistance measurement, as the size of the slide is significantly larger than the spacing between the probes.

## UV-Vis-NIR data processing

Reflection and transmission spectra were measured at normal incidence and were assumed to be entirely specular and incoherent. This assumption is reasonable as long as surfaces and interfaces scatter a minimal amount of light, and interference fringes in the spectra are minimal. At any wavelength/energy, the raw reflection ( $R_0$ ) and transmission ( $T_0$ ) of the blank substrate can thus be related to the reflectivity/transmissivity ( $R_g/T_g$ ) of the glass-air interface, and to the single-pass transmission of the glass substrate ( $X_g$ ) using the following equations:

$$R_0 = R_g + \frac{R_g X_g^2 T_g^2}{1 - R_g^2 X_g^2}$$

$$T_0 = \frac{X_g T_g^2}{1 - R_g^2 X_g^2}$$

$$1 = R_g + T_g$$

These equations can be solved for  $R_g$ ,  $T_g$ , and  $X_g$ .

Since a thin film on a glass substrate is a multilayer system, additional assumptions are needed to process the film/glass spectra analytically. In this work, the refractive indices of the film and substrate were both expected to be  $\sim 1.5$ , and thus the reflection at the film-glass interface could be ignored without significant distortion of the result. This simplification allowed for the raw reflection ( $R_1$ ) and transmission ( $T_1$ ) of the film/substrate to be incorporated into a similar set of equations as above while introducing only three new parameters:

$$R_1 = R_f + \frac{R_g X_g^2 X_f^2 T_f^2}{1 - R_g R_f X_g^2 X_f^2}$$

$$T_1 = \frac{X_g X_f T_g T_f}{1 - R_g R_f X_g^2 X_f^2}$$

$$1 = R_f + T_f$$

In this second set of equations,  $R_f$  and  $T_f$  are the reflectivity and transmissivity of the film-air interface, respectively, and  $X_f$  is the single-pass transmission of the thin film. Solving these equations for  $X_f$  gives the corrected transmission of the thin film. The corresponding absorption of the film is:

$$Abs_{film} = -\log(X_f)$$

This quantity can be calculated at each measured wavelength/energy to give the corrected absorption spectrum of the film.

## Pseudomobility

Conventional theory describes the conductivity ( $\sigma$ ) of doped semiconductors as the product of the elementary charge ( $e$ ), the density of positive charge carriers ( $\rho_h$ ), and the mobility of these same charge carriers ( $\mu$ ). In numerous examples,  $\rho_h$  is treated as an independent variable programmed by doping fraction, while  $\mu$  is an intrinsic material property found to vary with temperature, applied voltage, disorder, and doping fraction<sup>31,32</sup>.  $\mu$  thus encompasses most of the complexity of  $\sigma$  and is often maximized in order to optimize the performance of electronic materials. In the specific case of a hole transport material (HTM), the doping fraction must be managed carefully given that under-doping reduces hole conductivity, while over-doping risks depletion of valence electrons at the HTM/absorber interface that can lead to inefficient hole injection.

In this work, the value of  $\mu$  for each HTM film was extracted from sheet resistance 4-point probe and UV-Vis measurements using the following methodology.

The hole mobility of the HTM is expressed as:

$$\mu_h = \frac{\sigma}{\rho_h e}$$

where the hole conductivity of the HTM is assumed to approximate the total conductivity due to the heavy p-doping of most measured conditions and the high intrinsic mobility of holes relative to that of electrons known to exist in spiro-OMeTAD.  $\sigma$  is defined as:

$$\sigma = (R_s \cdot t)^{-1} = \left( \left( \frac{dV}{dI} \cdot C \cdot \pi \cdot t \right) / \ln(2) \right)^{-1}$$

where  $R_s$  is the sheet resistance,  $t$  is the film thickness,  $dV/dI$  is the linear change in voltage ( $V$ ) with respect to current ( $I$ ) at low  $V$  and  $I$  extracted from the 4-point probe measurement, and  $C$  is a geometric correction factor tied to the ratio

between the probe tip distances and the rectangular dimensions of the film. The redefinition of  $R_s$  here is valid for any 4-point probe measurement in which  $t$  is significantly less than the distance between adjacent probe tips.  $\rho_h$  is defined as:

$$\rho_h = \rho_{HTM} \cdot \frac{[HTM^+]}{[HTM]}$$

where  $\rho_{HTM}$  is the total density of redox active HTM sites in the film and  $[HTM^+]/[HTM]$  is the fraction of active sites carrying a positive charge at any given time. This fraction is not necessarily equal to the ratio of dopant to HTM in the film, since not all dopants oxidize HTM material quantitatively.  $\rho_{HTM}$  can be converted to a molar concentration by:

$$\rho_{HTM} = 1000 \cdot N_A \cdot [HTM]$$

where  $N_A$  is the Avogadro constant and  $1000 N_A$  is the unit of conversion between  $m^{-3}$  and M. The ratio of  $[HTM^+]$  to  $[HTM]$  is the same as the ratio of  $\rho_h$  to  $\rho_{HTM}$ . This yields:

$$\rho_h = 1000 \cdot N_A \cdot [HTM^+]$$

which can be used in conjunction with Beer's law to incorporate data from the UV-Vis spectrum of the film in question. The resulting equation:

$$\rho_h = 1000 \cdot N_A \cdot \frac{Abs_{HTM^+}}{\epsilon \cdot t} = 1000 \cdot N_A \cdot \frac{Abs_{film}}{\epsilon \cdot t}$$

includes the molar extinction coefficient of the film ( $\epsilon$ ), the film thickness ( $t$ ), and the reflection- and substrate-corrected absorbance ( $Abs_{HTM^+}$ ) of the film in the wavelength range of  $500 \pm 5$  nm, where all absorption can be attributed to  $HTM^+$ . This final expression for  $\rho_h$  is only valid when the programmed dopant:HTM ratio is at or below 1:1 so that minimal  $HTM^{2+}$  exists in the film. Finally,  $\mu_h$  can be defined in terms of both experimental results:

$$\mu_h = \frac{\sigma}{\rho_h e} = \left( \frac{\ln(2) \cdot \epsilon}{1000 \cdot \pi \cdot e \cdot C \cdot N_A} \right) \left( \frac{dI}{dV} \right) (Abs_{HTM^+})^{-1}$$

This expression is crucially independent of film thickness, allowing for accurate optimization over the full compositional and processing variable space employed in this work. Dividing out the constants in the final equation above yields a parameter termed pseudomobility:

$$pseudomobility = \left( \frac{dI}{dV} \right) (Abs_{HTM^+})^{-1}$$

Pseudomobility is equivalent to the quotient of film conductivity and p-type carrier density and provides a useful measure of relative mobility that can be utilized in optimization experiments.

# Supplementary Tables

## Sample data table for each campaign

**Supplementary Table 1 | Values of manipulated and responding variables for run 1.**

Sample	Dopant:HTM (mol:mol)	Annealing time (s)	Conductance (nS)		HTM <sup>+</sup> Absorptance at 500 nm		Pseudomobility (nS)	
			<i>mean</i>	<i>st. dev.</i>	<i>mean</i>	<i>st. dev.</i>	<i>mean</i>	<i>st. dev.</i>
0	0.358	115	7.6	20.0	0.079	0.050	47	124
1	0.994	202	50.7	3.3	0.324	0.020	157	19
2	0	237	0.0	0.0	0.001	0.000	0	0
3	0.761	133	0.0	0.0	0.067	0.004	0	0
4	0.979	1	35.9	0.3	0.258	0.006	139	3
5	0.987	227	41.8	17.9	0.314	0.038	136	59
6	0.046	2	4.2	0.1	0.026	0.000	161	4
7	0.994	216	42.2	9.6	0.329	0.033	129	30
8	0	0	0.0	0.0	0.005	0.002	0	0
9	0.178	21	39.2	0.9	0.086	0.003	458	23
10	0.491	0	60.8	2.0	0.183	0.004	332	11
11	0.341	49	73.8	20.5	0.135	0.002	548	156
12	0.394	3	52.2	17.4	0.153	0.003	341	114
13	0.444	23	66.5	25.9	0.163	0.006	410	165
14	0.025	128	3.9	0.4	0.022	0.003	184	25
15	0.402	76	120.7	1.1	0.164	0.003	734	13
16	0.458	238	0.0	0.0	0.055	0.002	0	0
17	0.409	92	16.6	28.6	0.102	0.049	98	168
18	0.522	88	10.7	24.4	0.098	0.048	60	129
19	0.395	69	74.5	36.2	0.152	0.009	485	237
20	0.389	73	109.8	10.1	0.160	0.003	685	52
21	0.387	81	47.4	54.0	0.142	0.038	281	319
22	0.975	88	68.0	0.8	0.357	0.196	218	59
23*	0.376*	72*	104.0*	18.4*	0.044*	0.014*	2,600*	935*
24	0.345	73	55.9	54.8	0.153	0.008	355	347
25	0.308	82	58.1	39.3	0.139	0.006	421	281
26	0.529	172	0.0	0.0	0.073	0.010	0	0
27	0.372	70	94.9	42.9	0.163	0.003	580	261
28	0.685	75	10.4	27.6	0.129	0.064	51	134

29	0.315	63	102.4	2.5	0.141	0.004	727	13
30	0.235	167	4.5	11.8	0.090	0.030	34	90
31	0.337	72	60.8	42.0	0.138	0.021	427	262
32	0.31	81	97.7	11.1	0.141	0.008	692	74
33	0.45	58	126.6	1.5	0.180	0.003	703	10
34	0	93	0.0	0.0	0.002	0.000	0	0

\*A brief spectrometer power failure resulted in calibration errors between the spectra of the glass slide and the spectra of the thin film, invalidating the calculation of thin film absorptance. This outlier was removed in all following analyses.

**Supplementary Table 1 | Values of manipulated and responding variables for run 2.**

Sample	Dopant:HTM (mol:mol)	Annealing time (s)	Conductance (nS)		HTM <sup>+</sup> Absorptance at 500 nm		Pseudomobility (nS)	
			<i>mean</i>	<i>st. dev.</i>	<i>mean</i>	<i>st. dev.</i>	<i>mean</i>	<i>st. dev.</i>
0	0.988	202	53.5	3.0	0.354	0.013	152	13
1	0.359	115	9.3	24.6	0.082	0.044	58	154
2	0.702	151	0.0	0.0	0.067	0.003	0	0
3	0.032	4	2.4	0.1	0.019	0.000	122	3
4	0.904	175	77.6	6.4	0.300	0.009	259	29
5	0.927	233	46.0	28.6	0.285	0.084	190	134
6	0.973	206	39.0	21.6	0.299	0.056	139	92
7	0	237	0.0	0.0	0.008	0.016	0	0
8	0.967	212	48.9	38.7	0.284	0.102	241	245
9	0.98	1	39.3	0.1	0.275	0.002	143	1
10	1.009	147	39.8	27.1	0.290	0.068	161	144
11	0.543	0	78.5	0.5	0.204	0.003	384	5
12	1.026	159	49.4	16.9	0.318	0.016	155	54
13	0.516	1	76.9	1.2	0.192	0.005	399	5
14	0.535	43	125.6	1.0	0.219	0.005	574	15
15	0.491	0	71.0	1.7	0.189	0.008	376	21
16	0.504	58	88.2	53.4	0.190	0.007	457	272
17	0.023	127	3.7	0.1	0.023	0.001	158	2
18	0.567	67	47.3	55.9	0.170	0.051	225	260
19	0.508	233	0.0	0.0	0.055	0.004	0	0
20	0.464	47	131.5	1.3	0.185	0.003	712	6
21	0.592	59	100.6	36.7	0.191	0.035	515	151
22	0.472	41	130.2	1.6	0.184	0.002	707	14
23	0.337	70	108.5	7.4	0.155	0.009	701	27
24	0.482	62	126.7	15.4	1.556	2.310	438	287

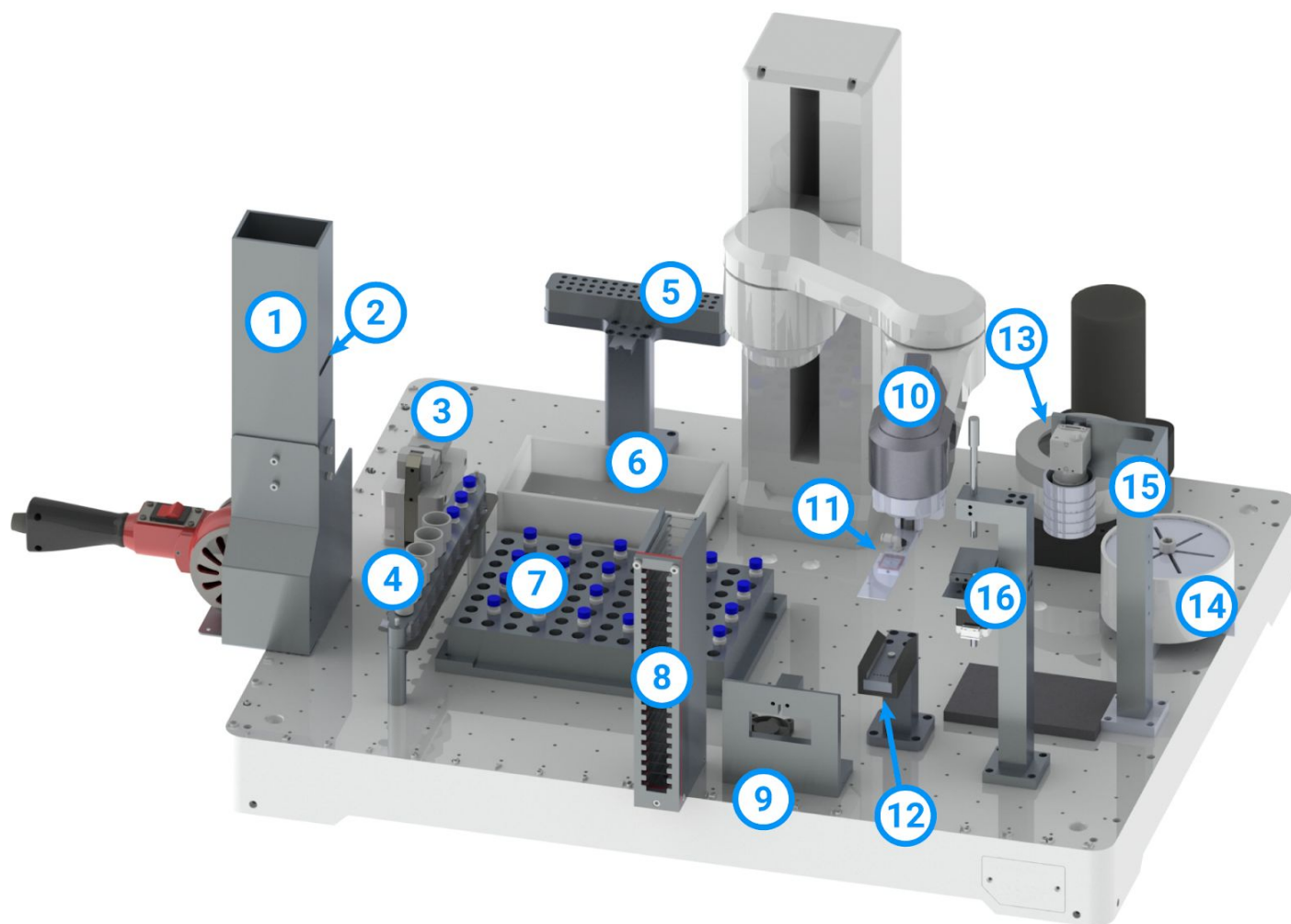
25	0.314	70	107.3	5.6	0.149	0.008	722	42
26	0.441	50	133.3	0.4	0.182	0.002	734	7
27	0.239	79	57.5	39.9	0.122	0.001	470	326
28	0.469	66	47.4	51.2	0.154	0.039	269	277
29*	0.292*	57*	0.0*	0.0*	0.001*	0.000*	0*	0*
30	0.313	28	92.7	1.3	0.138	0.003	671	11
31	0.329	58	109.0	2.7	0.146	0.003	745	18
32	0.367	19	87.1	0.9	0.148	0.002	587	13
33	0.247	59	88.9	0.6	0.119	0.001	748	7
34	0.314	34	90.5	3.7	0.127	0.007	717	54

\*An alignment error during spin coating resulted in no precursor solution deposited onto the glass slide. This outlier was removed in all following analyses.

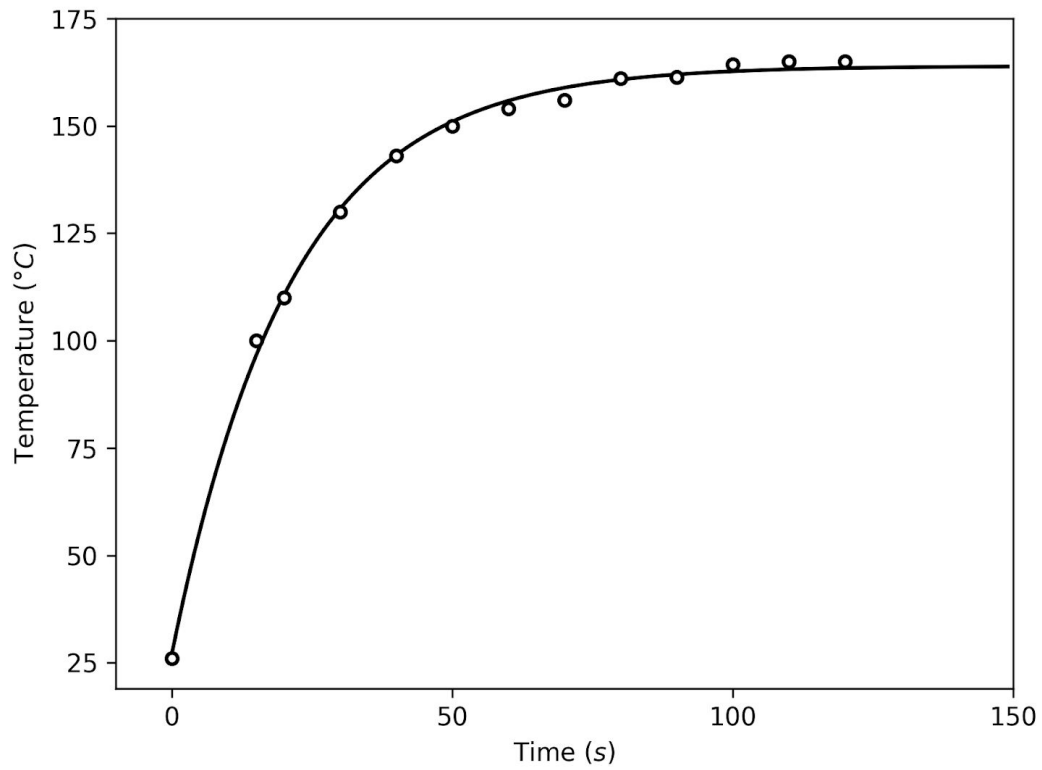
# Supplementary Data

## Supplemental figures

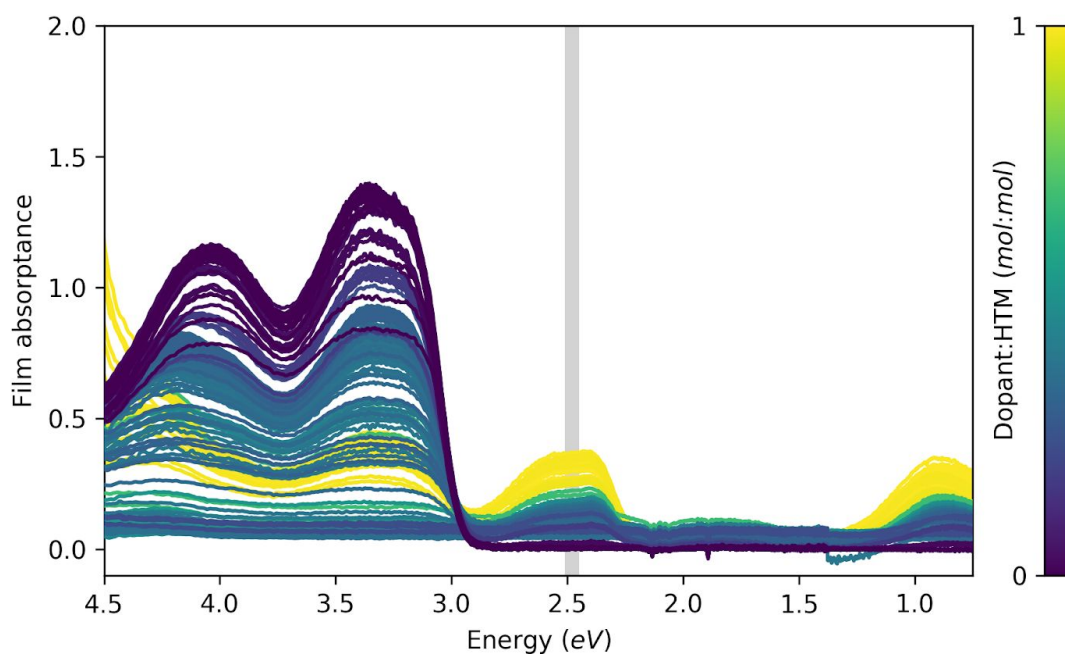
All figures containing numerical data were created in Python using the matplotlib library<sup>33</sup>.



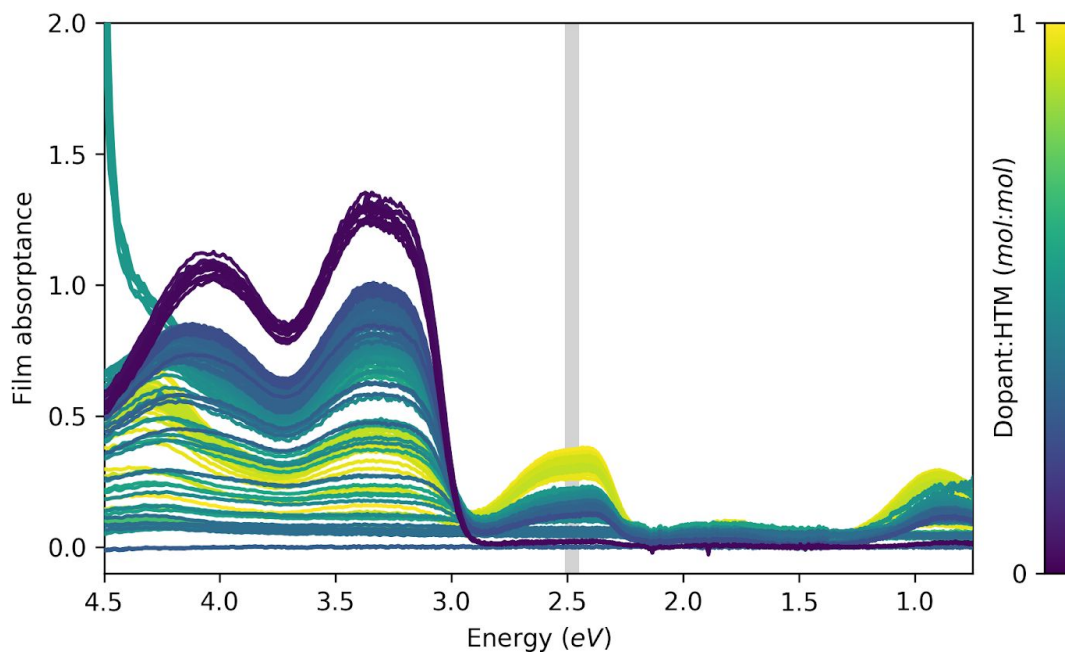
**Supplementary Fig. 1 | *Ada* fabricates and characterizes thin films on a single robotic platform.** This platform includes: (1) an annealing furnace with (2) a slot-shaped sample port; (3) a weigh scale for feedback dispensing of solutions; (4) a rack for stock solution vials; (5) a rack for storing clean pipet tips and (6) a container for disposal of used tips; (7) a rack for clean mixing vials; (8) a rack for clean glass slides; (9) a 4-point probe for measuring film conductance; (10) a robotic arm for handling vials and slides with (11) an attachment for gripping slides and (12) a station for storing this attachment when not in use; (13) a spin coater with (14) a removable lid; (15) a camera for dark field imaging; (16) a spectrometer for transmission and reflection measurements.



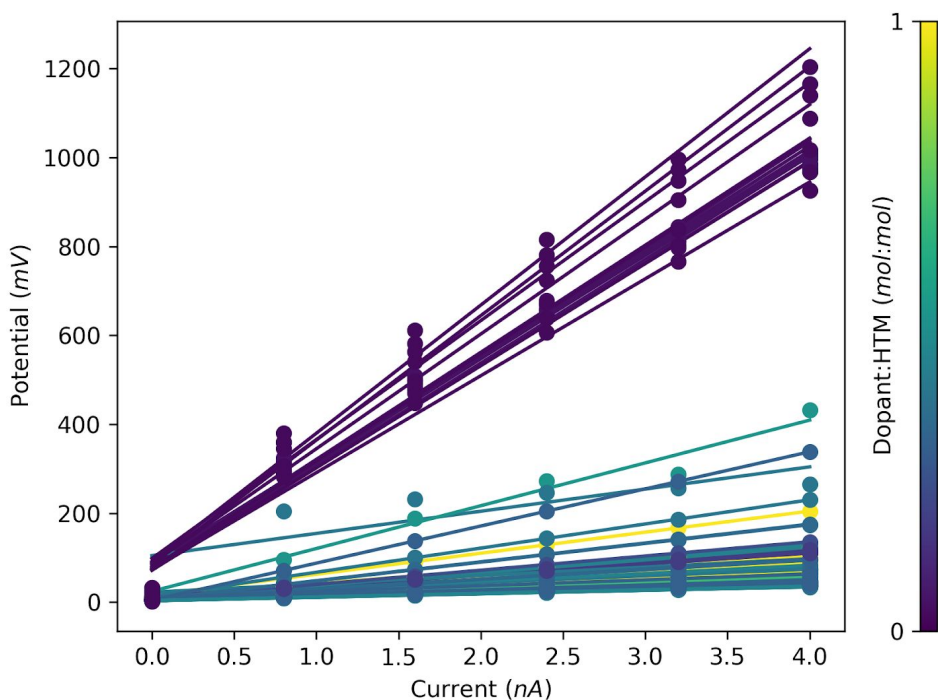
**Supplementary Fig. 2 | Temperature profile of the heating protocol employed by *Ada's* annealing furnace.** A thermocouple was contacted to a glass microscope slide and the measured temperature was collected at a series of times after the heat gun was turned on. The data was fit to an asymptotic regression model.



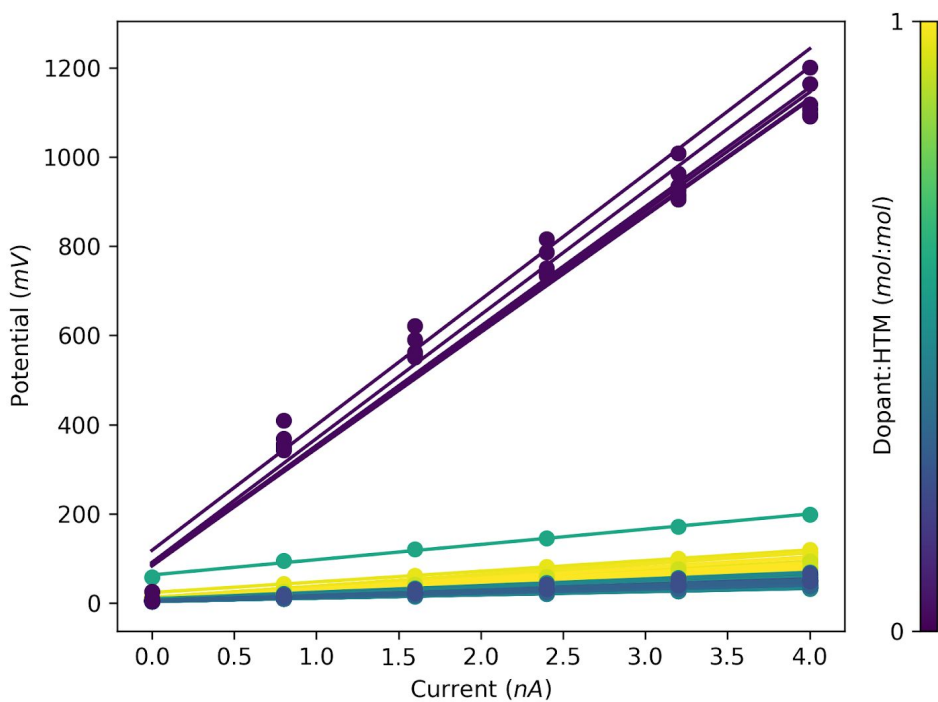
**Supplementary Fig. 3 | UV-Vis-NIR film absorbance spectra for run 1.** The film absorption was calculated from the transmission and reflection spectra of both the glass substrate and the deposited film on the glass substrate. Absorption values for films with varying dopant:HTM ratios are shown, as indicated by the side bar. The mean absorption from 495 - 505 nm (indicated by the grey bar) was used to calculate pseudomobility.



**Supplementary Fig. 4 | UV-Vis-NIR film absorbance spectra for run 2.** The film absorption was calculated from the transmission and reflection spectra of both the glass substrate and the deposited film on the glass substrate. Absorption values for films with varying dopant:HTM ratios are shown, as indicated by the side bar. The mean absorption from 495 - 505 nm (indicated by the grey bar) was used to calculate pseudomobility.

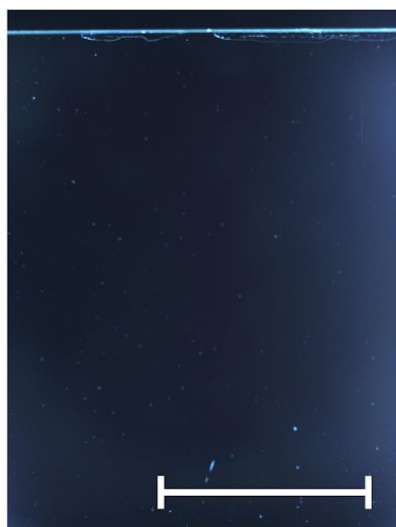


**Supplementary Fig. 5 | Current-voltage relationships for run 1.** Potentials were recorded with a 4-point probe delivering a current between 0 and 4 nA for films with varying dopant:HTM ratios as indicated by the side bar. Conductance was calculated from the fitted slope of the current-voltage plots.



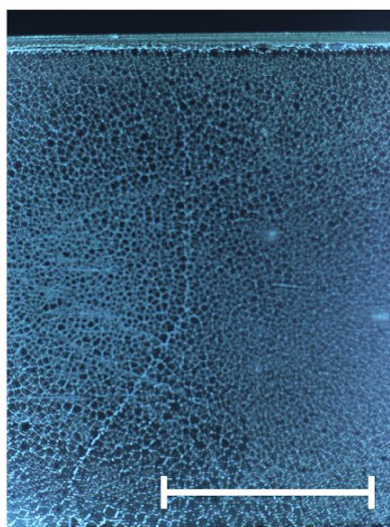
**Supplementary Fig. 6 | Current-voltage relationships for run 2.** Potentials were recorded with a 4-point probe delivering a current between 0 and 4 nA for films with varying dopant:HTM ratios as indicated by the side bar. Conductance was calculated from the fitted slope of the current-voltage plots.

Increasing Dopant:HTM



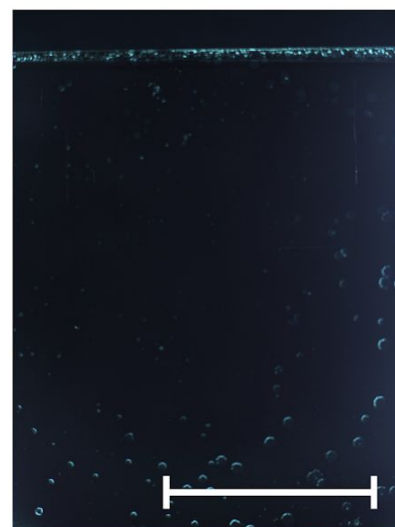
**Sample 7**

Dopant:HTM = 0 mol:mol  
Annealing time = 237 s



**Sample 19**

Dopant:HTM = 0.508 mol:mol  
Annealing time = 233 s



**Sample 5**

Dopant:HTM = 0.927 mol:mol  
Annealing time = 233 s

**Supplementary Fig. 7 | Dark field images of highly annealed spiro-OMeTAD thin films with different ratios of dopant.** Shown above are the images of three representative samples from run 2. When no dopant was added, no dewetting was observed. Dewetting was much more significant at an intermediate dopant:HTM ratio compared to a high dopant:HTM ratio. Scale bars are 1 cm.

## References

31. Liu, C. *et al.* A unified understanding of charge transport in organic semiconductors: the importance of attenuated delocalization for the carriers. *Mater. Horiz.* **4**, 608–618 (2017).
32. Shen, Y. *et al.* Charge transport in doped organic semiconductors. *Phys. Rev. B Condens. Matter* **68**, 081204 (2003).
33. Hunter, J. D. Matplotlib: A 2D Graphics Environment. *Computing in Science Engineering* **9**, 90–95 (2007).